Laser-driven shock waves studied by X-ray radiography

L. Antonelli,* S. Atzeni, and A. Schiavi
Dipartimento SBAI, Università degli Studi di Roma "La Sapienza", Via Antonio Scarpa 14, 00161, Roma, Italy

S. D. Baton, E. Brambrink, and M. Koenig
Laboratoire LULI Ecole Polytechnique, 91128, Palaiseau Cedex, France

C. Rousseaux
CEA, DAM, DIF, F-91297 Arpajon, France

M. Richetta
Dipartimento di Ingegneria Industriale, Università degli Studi di Roma "Tor Vergata", Via del Politecnico 1, 00133, Roma, Italy

D. Batani, P. Forestier-Colleoni, E. Le Bel, Y. Maheut, T. Nguyen-Bui, X. Ribeyre, and J. Trela
Université de Bordeaux, CNRS, CEA, CELIA (Centre Lasers Intenses et Applications), UMR 5107, F-33405 Talence, France
(Dated: May 19, 2017)

Multi-megabar laser-driven shock waves are unique tools for studying matter under extreme conditions. Accurate characterization of shocked matter is for instance necessary for measurements of equation of state data or opacities. This paper reports experiments performed at LULI facility on the diagnosis of shock waves, using X-ray absorption radiography. Radiographs are analyzed using standard Abel inversion. In addition, synthetic radiographs, which also take into account the finite size of the X-ray source, are generated using density maps produced by hydrodynamic simulations. Reported data refer to both plane cylindrical targets and hemispherical targets. Evolution and deformation of the shock front could be followed using hydrodynamic simulations.

I. INTRODUCTION

The generation of multi-Mbar shock waves in the interaction of high power lasers with solid matter [1–4] allows studies of matter at extreme conditions [5, 6]. In particular, we refer to the so-called warm dense matter (WDM) and hot dense matter (HDM), relevant to astrophysics, material science as well as Inertial Confinement Fusion (ICF) [7, 8]. The strongly coupled and degenerate states of matter in those conditions make their description far from ideal. In order to discriminate between different theoretical models, accurate measurements are needed.

Most of the available large scale facilities allow to study compression in plane geometry only. However high pressure in plane geometry with laser of moderate pulse energy (< 1 kJ) requires a small focal spot to maximize the intensity on target, and this leads to two-dimensional (2D) effects and lateral dispersion of the energy during the propagation of the shock wave over distances comparable or longer than the focal spot size. The non-uniformity of the shock front hinders accurate shock diagnosis. In this context, we performed an experiment at the LULI laser facility aiming at the accurate detection of shape and position of a strong laser-driven shock wave. We examined two different laser-target configurations. In the first one we irradiated a plane surface, while in the second one a hemisphere. We used two-dimensional X-ray absorption radiography to obtain an image of the shocked target and, in particular, of the shock wave front. This technique was already used in the past at the same laser facility [9–13] and elsewhere (e.g. [14, 15]). Streaked radiography (i.e. time-resolved one-dimensional radiography) is also used to measure converging shock speed in spherical targets [16, 17].

In our work we also developed a specific post-processing module coupled to the hydrodynamic code DUED [18], which allows us to compare directly the experimental results with the numerical density maps. The new module calculates a synthetic radiograph taking into account the finite X-ray source dimensions and its spatial distribution, which can play a non-negligible role. Indeed, the standard Abel inversion method (which relies on plane wave front) cannot take into account the spatial properties of the backlighting source. The Abel inversion of experimental data is also intrinsically noisy due its mathematical formulation. Therefore it requires a fitting and filtering procedure, which can wipe out a significant amount of information contained in experimental data. We show instead that with our new approach we can obtain a satisfactory reproduction of experimental data.

II. EXPERIMENTAL SETUP

The experimental setup is represented in Fig. 1. The laser pulse of LULI2000 was focused on a CH plastic target to generate a strong shock wave which was characterized using X-ray absorption radiography. X-rays were generated by a Vanadium backlighter irradiated by the

* luca.antonelli@uniroma1.it; luca.antonelli.1985@gmail.com

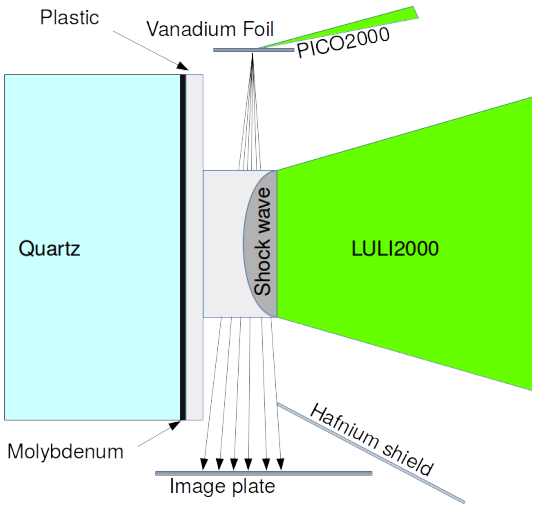

FIG. 1. Sketch of the experimental setup.

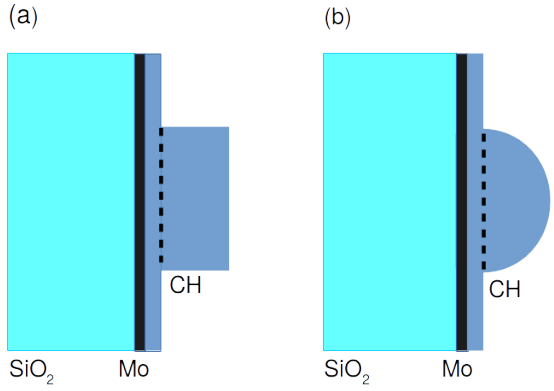

FIG. 2. (a) Cylindrical target with a flat interaction surface; (b) hemispherical target.

PICO2000 laser.

A. Laser

LULI2000 is a Nd:glass laser delivering up to 500 J in second harmonic ($2\omega = 526$ nm) in 2 ns with flat-top temporal profile (see Sec. III for details). PICO2000 Nd:glass laser can deliver up to 40 J in second harmonic ($2\omega = 526$ nm) with a Gaussian pulse duration of about 3 ps.

The LULI2000 ns laser pulse was focused using a Random Phase Plate (RPP), producing a nominal Gaussian focal spot with 330 μm FWHM. The resulting intensity on target was in the order of 10^{14} Wcm^{-2}. However, the actual laser spot - measured using a different CW laser - varied significantly from shot to shot and was typically smaller than the nominal one. Also, it showed significant departures from cylindrical symmetry. In the simulations presented in the following we assumed a (cylindrically symmetrical) Gaussian focal spot with 200 μm FWHM.

B. Targets

Two different layered targets were used, as depicted in Fig. 2 (a) and (b). Both targets had a front plastic layer (polypropylene) for laser interaction and shock wave propagation with two different shapes. A cylinder with radius of 250 μm and length of 250 μm (a) and a half sphere with radius of 250 μm (b). A middle layer of 15 μm Molybdenum was used to shield the streak cameras (for VISAR [19] and streaked optical pyrometry, SOP [1]) from direct laser illumination. Also it was intended to mitigate the pre-heating of the material ahead the shock due to X-rays and hot electrons. A layer of quartz was used to measure the shock velocity using a VISAR [6]; VISAR measurements are not discussed in this paper.

C. X-ray radiography

The main diagnostic technique was X-ray absorption radiography. The PICO2000 beam was focused onto a 10 μm thick Vanadium foil to produce an intense X-ray pulse. The interaction between the intense laser beam and the target generates hot electrons, which excite the inner shell electrons of Vanadium producing K_α radiation, with energy of 4.9 keV. We recorded this K_α radiation using a Germanium crystal in Von Hamos configuration [20, 21]. To record the radiograph we used an Image Plate placed 28 cm away from the target. The distance between the X-ray source and the target was 0.8 cm. The expected magnification was therefore 35 times. The X-ray absorption setup was tested by irradiating a hemispherical target with radius of 250 μm (see Fig. 3 and the discussion in the next subsection). The synchronization between LULI2000 and PICO2000 had a jitter of 100 ps.

Data treatment and analysis

Radiography generates a map of X-ray transmission (ratio of transmitted intensity to incident intensity) through the target. Using this information one can reconstruct the density map of the target under certain conditions [22]. Assuming cylindrical geometry the incident X-ray intensity $I(y,z)$ (with z the target symmetry axis and y the distance from it in the experimental image) is described by

$$I(y,z) = I_0 \exp\left(-\int_{-x_0}^{+x_0} k(E,x,y,z)dx\right), \qquad (1)$$

where I_0 is the back-lighter intensity (in the experiment obtained for each radiograph from the unattenuated X-ray signal). The attenuation coefficient k depends on the X-ray energy E and material according to

$$k(E,x,y,z) = \mu(E,x,y,z)\rho(x,y,z), \tag{2}$$

where μ is the mass attenuation coefficient characteristic of the specific material, and ρ is the material density. We can then calculate

$$-\ln\left(\frac{I}{I_0}\right) = 2\int_0^{+x_0} k(E,x,y,z)dx. \tag{3}$$

Changing variable from x to r, $x = \sqrt{r^2-y^2}$, we finally have

$$-\ln\left(\frac{I}{I_0}\right) = 2\int_y^{+\infty} \frac{k(E,r,z)rdr}{\sqrt{r^2-y^2}}. \tag{4}$$

We can apply Abel inversion to obtain the attenuation coefficient from Eq.(4), which gives

$$k(E,r,z) = \frac{1}{\pi}\int_r^{+\infty} \frac{d}{dx}\left[\ln\left(\frac{I(y,z)}{I_0}\right)\right]\frac{dy}{\sqrt{y^2-r^2}}, \tag{5}$$

where r is the distance of the point of the image from the symmetry axis z in the inverted image. Due to the assumption of cylindrical symmetry, only half of the image is actually used in the inversion process. Assuming a mass attenuation coefficient μ depending only on the X-ray energy (which is appropriate in the range of density and temperature considered in our experiment [22]) one can obtain the density map of the target from Eq.(2). In our case (for 4.9 keV photons in plastic) $\mu \approx 18.5$ cm^2/g [23]. We developed a program to compute the *Abel inversion* of the experimental transmission map to retrieve the density map. We also developed a module which computes the *Abel transform* to obtain a transmission map from a given density map.

In addition, we produced numerical density maps, which can be compared with experimental data. We used the 2D, two-temperature radiation hydrodynamic code DUED. Equation of state data are provided by a slightly improved version of the model of Ref. [24]. We have checked that DUED with the quoted EOS reproduces with high accuracy the experimental data [25] for plastic at pressures in the range 1-10 Mbar. Radiative transfer is described by a multi-group diffusion scheme. Opacities are provided by an upgraded version of the SNOP code [26]. While the original SNOP code only applies to single-element materials, the present version, developed at Roma-La Sapienza, also deals with mixtures. Moreover, we developed a module which can calculate a synthetic radiograph using the numerical density map. In this way we were able to include important source properties such as the finite width of the X-ray source which cannot be included in a simple Abel treatment.

The whole procedure was tested in the case of the non-irradiated hemispherical target. Fig. 3 shows the experimental radiograph (a), the synthetic radiograph (b) and the Abel transform (c). Figure 4 shows transmission vs axial coordinate z, as obtained from the experimental radiograph, the synthetic radiograph and Abel transform. The error bars are estimated from the fluctuations of the backlighting source, which gives the dominant contribution to the noise. In the synthetic radiograph an X-ray source with Gaussian intensity distribution and 30 μm FWHM was assumed. Such a value of the K_α source size is larger than the laser spot size, as reported in previous experiments [27]. Figure 4 shows how the source width plays a fundamental role. Unlike the experimental data, the Abel transform shows a sharp edge at the target border and underestimates transmission. The effect of the X-ray source size will be discussed in more detail in Sec. III A.

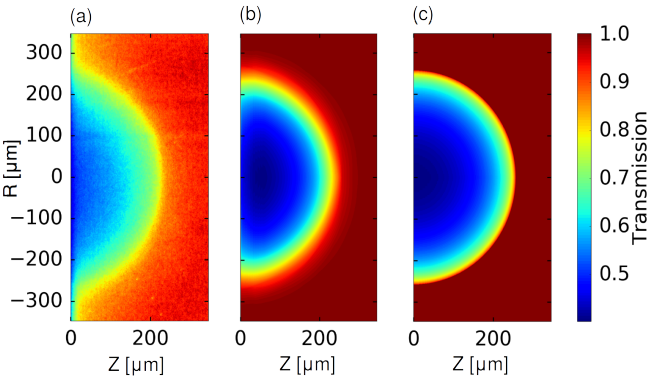

FIG. 3. Radiography test of a hemispherical target (a), compared with a synthetic radiograph (b) and the Abel transform of the numerical density map (c).

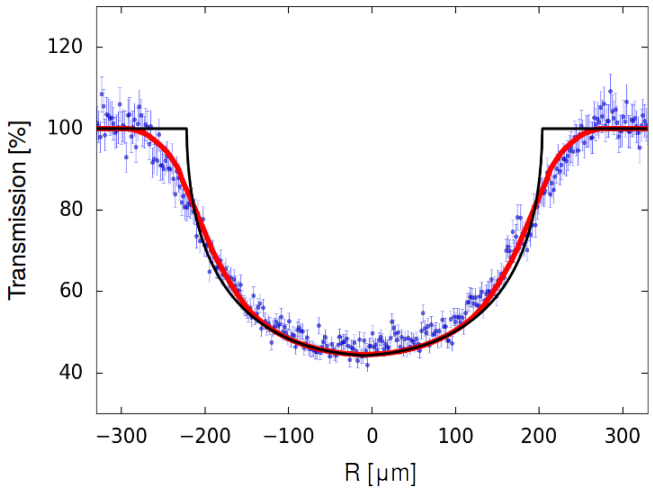

FIG. 4. Transmission of the hemispherical target along the line $z = 130$ μm. The experimental result (dots) is compared with the synthetic radiograph (red curve) and Abel transform of the numerical density map (black curve).

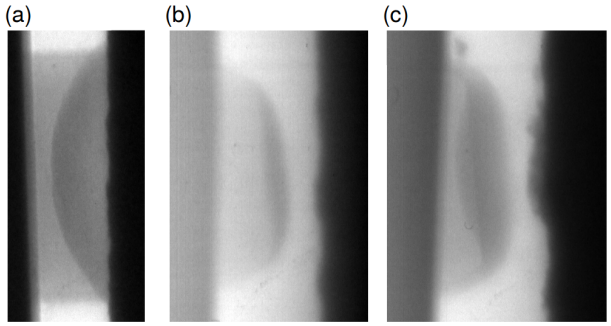

FIG. 5. Experimental radiographs. (a) Cylindrical target at t = 4.7 ns; (b) and (c) spherical target at $t = 2.7$ ns and $t = 4.7$ ns, respectively.

III. RESULTS

We applied our 'simulation-assisted' radiography technique to the data collected in the experiment for the cylindrical target and then for the hemispherical target. The raw data for both targets are shown in Fig. 5. Notice that all images are not symmetrical with respect to the z-axis. In the case of hemispherical targets, in addition, the shock front is clearly slightly tilted with respect to the same axis. Since our procedure requires cylindrical symmetry, we rotated these images. In all cases, we used half an image (the upper portion). We checked that using the lower portion leads to similar results.

A. Cylindrical target

We consider a shot in which the laser delivered 400 J in second harmonic with a flat-top of 1.2 ns, preceded by a linear rise in 0.4 ns and followed by a linear decrease in 1.2 ns. The picosecond pulse was delayed by 4.7 ns from the start-time of the nanosecond pulse. Figure 6 shows the experimental radiograph (a) together with the synthetic radiograph (b). The synthetic radiograph was generated by post-processing a DUED hydrodynamic simulation, using nominal laser power (and hence energy), and a Gaussian focal spot with 200 μm FWHM. The comparison of Figs. 6(a) and (b) shows a good general agreement. Notice however that the experimental image is not exactly symmetric; also, the curvature of the shock front in the two images is slightly different. The experimental image is flatter about the axis than the simulated one. Unfortunately, lack of information on the actual shape of the laser spot does not allow to ascertain the origin of this discrepancy. In Fig. 6, as well as in all following figures, the origin of the z-axis coincides with the base of the cylinder or the base of the hemisphere; see the dashed vertical lines in Fig. 2.

In the same experiment, the transit time of the shock wave through the plastic and Molibdenum layers was

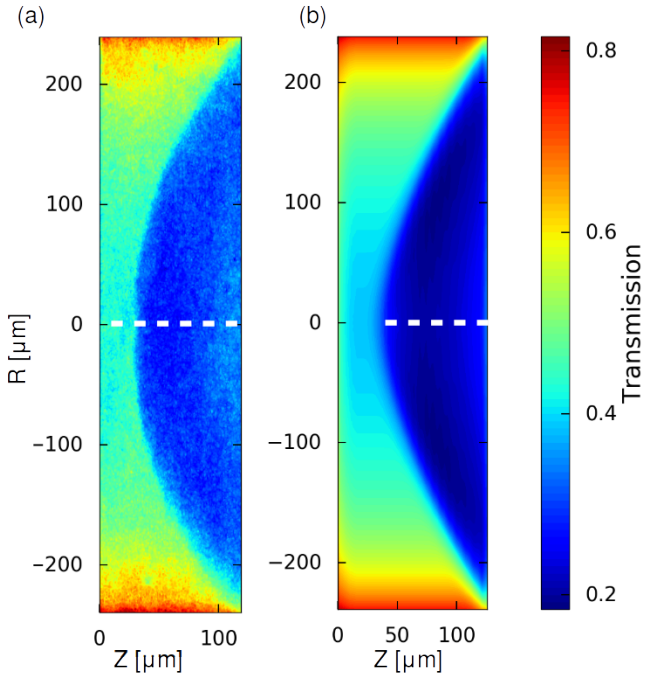

FIG. 6. Shock wave in the cylindrical target: (a) experimental radiograph; (b) synthetic radiograph. The laser pulse driving the shock comes from the right hand side.

measured by SOP, observing the visible light emitted from the rear surface of the Molibdenum layer. The shock was found to break-out at time $t_{\rm bo} = 8.5$ ns.

A more quantitative comparison between experiment and simulation is shown in Fig. 7, referring to the X-ray transmission along the symmetry axis. We find that the simulated curve, shifted by 7 μm to the left hand side, overlaps to the experimental one within experimental errors.

In the previous synthetic radiographs we assumed a X-ray Gaussian source with 30 μm FWHM. In Fig. 8 we show how the source size affects transmission. It is seen that the curves differ sensibly in correspondence to the shock front. FWHM's in the range 20–40 μm are roughly consistent with experimental data.

On the basis of the good agreement between the experimental data and the simulated ones, we can estimate several quantities using the detailed information (such as maps of density, electron and ion temperature, pressure, etc.) provided by the numerical simulation. In Fig. 9(a)-(c) we show the density maps at times $t = 0.7$ ns, $t = 2.7$ ns and $t = 4.7$ ns, respectively. The density map at $t = 4.7$ ns is the same used in the synthetic radiograph and in the Abel transform. We notice how the shape of the focal spot affects the shock front. At $t = 0.7$ ns the shock front has the same radial extension as the laser focal spot. At $t = 2.7$ ns it is still flat in the center but curved at the edges. Finally, at $t = 4.7$ ns we observe a curved shock front similar to the experimental one.

It is also worth noticing that the shock break-out time

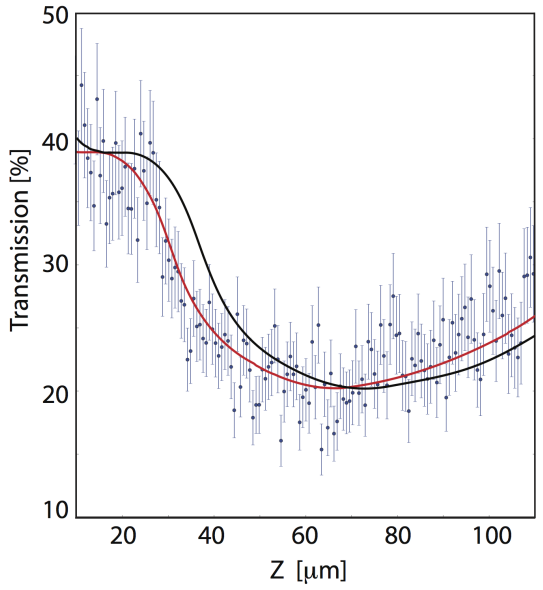

FIG. 7. Cylindrical target. Experimental transmission (dots, with error bars) and simulated transmission (black curve). The red curve is the simulated transmission curve shifted 7 μm to the left hand side.

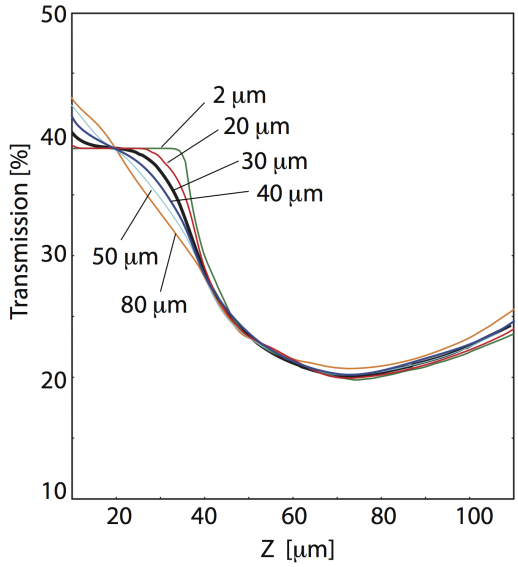

FIG. 8. Cylindrical target. Simulated transmission for different dimensions of the X-ray source. The labels in the figure refer to the source FWHM. The black curve is the same as in Fig. 7.

from the DUED simulation, $t_{\rm bo} \simeq 8.4$ ns, agrees with the experimental value.

From the simulation we can also infer the shock pressure from the hydrodynamic simulations. The highest pressure inferred is 20 Mbar (with a density ratio between the shocked and unshocked material of about 3.8) at the end of the laser pulse at $t = 2$ ns. At $t = 4.7$ ns the inferred pressure is about 8 Mbar (with a density ratio

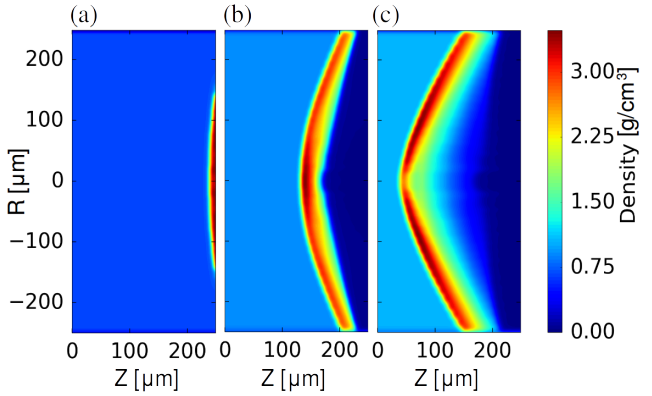

FIG. 9. Cylindrical target. Simulated density maps at times $t = 0.7$ ns (a), $t = 2.7$ ns (b), and $t = 4.7$ ns (c).

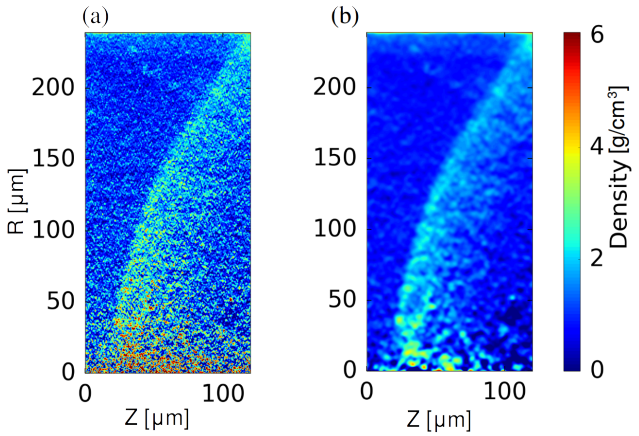

FIG. 10. Density maps from Abel inversion of the experimental radiograph shown in Fig. 6(a). (a) Abel inversion of the raw data; (b) Abel inversion applied after a Gaussian smoothing 2 pixel in radius of the raw data.

between the shocked and unshocked material of about 3.35).

From the experimental data we could obtain directly the density map using the Abel inversion described in section II C. The result is shown in Fig. 10 (a). The noise of the experimental data is considerably amplified by the transformation. One simple way to improve the reconstructed density map is to apply a digital filter to the experimental image to attenuate the noise. In Fig. 10(b) we show the map obtained using a Gaussian filter two pixel in radius on the experimental data before the Abel inversion. However, once we filter data, we have a loss of information. In particular, the sharp features of the shock front are lost, hindering the possibility to measure the compression ratio, and hence the strength of the shock wave. The above features are confirmed by Figs. 11 and 12, comparing density profiles along the line $r = 40$ μm from Abel inversion and from DUED simulations.

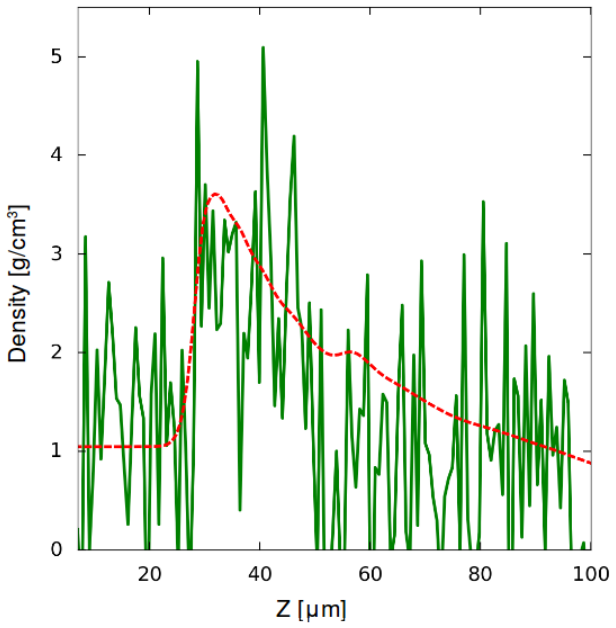

FIG. 11. Density profile along the line $r = 40$ μm. Abel transform of the raw experimental data (green curve) vs DUED simulation, shifted 7 μm to the left hand side (red dashed curve).

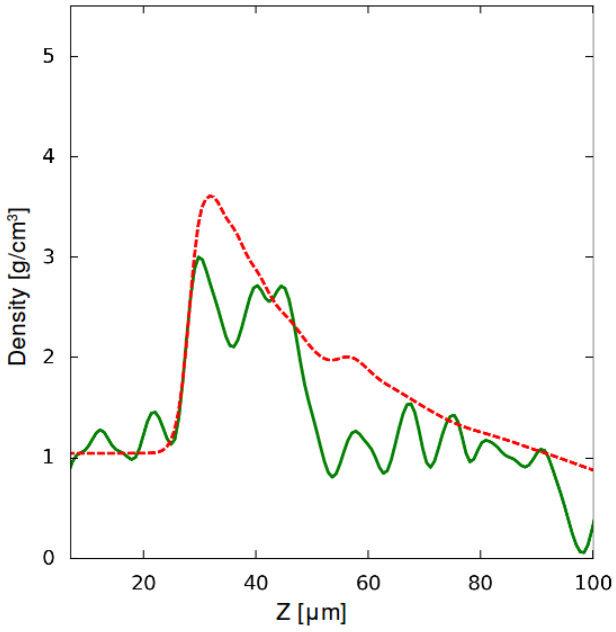

FIG. 12. Density profile along the line $r = 40$ μm. Abel transform of the filtered experimental data (green curve) vs DUED simulation, shifted 7 μm to the left hand side (red dashed curve).

B. Hemispherical target

With the hemispherical target, we acquired radiographs in two shots. In the first one (with laser energy $E_L = 450$ J) we acquired a radiograph at time $t = 2.7$ ns; in the second one ($E_L = 350$ J) we acquired a radiograph at $t = 4.7$ ns.

In Fig. 13 we show experimental data (top) and simulated ones (bottom). In the experiment, 3D effects were caused by laser mispointing. As already mentioned, to perform our analysis, we slightly rotated (≈ 3 degrees) both images. In the simulations we assumed a Gaussian focal spot with 200 μm FWHM. In both cases the laser energy was reduced to 80% of measured value, while the power time-dependence followed the experimental curve. (Using the measured value we obtain shock velocities 6-7% larger than the experimental ones.) Figure 13(a) shows a quite flat shock front at $t = 2.7$ ns, while Fig. 13(b) shows a curved shock front at $t = 4.7$ ns.

Experimental and simulated transmission profiles along the propagation axis at times $t = 2.7$ ns and $t = 4.7$ ns are presented in Figs. 14 and 15, respectively. The simulated curves overlap to the experimental ones within experimental errors. In the case of radiograph at $t = 2.7$ ns a better agreement is found by shifting the simulated curve by 5 μm to the right hand side.

As we already did for the cylindrical target, also for the hemispherical target we can understand the evolution of

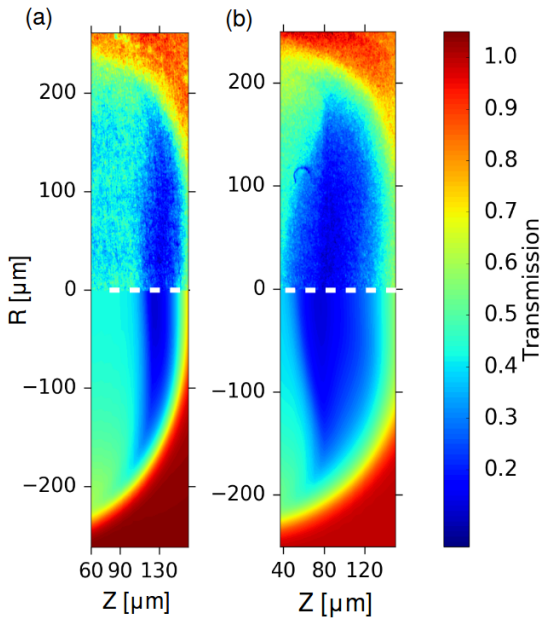

FIG. 13. Experimental radiographs (top) and synthetic radiographs (bottom) for the hemispherical target. The shock wavefront appears quite flat at 2.7 ns (a) and definitely curved at 4.7 ns (b).

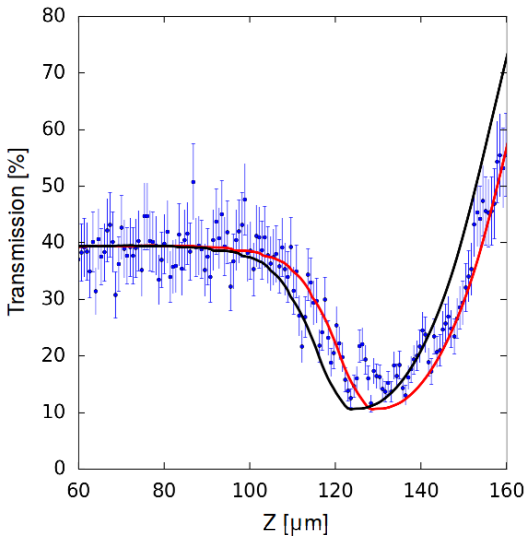

FIG. 14. Hemispherical target. Experimental transmission (dots) and simulated transmission (black curve) at $t = 2.7$ ns. The red curve is the simulated transmission curve shifted 5 μm to the right hand side.

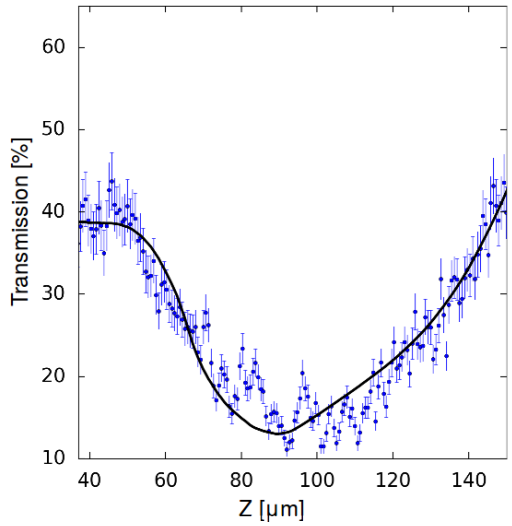

FIG. 15. Same as Fig. 14, at time $t = 4.7$ ns.

the shock wave using the simulations. DUED simulation results are shown in Fig. 16, for a case with laser energy $E_L = 280$ J. The simulation allows us to estimate the time interval during which the shock front is almost flat. In fact, the radiographs show a nearly flat front at $t = 2.7$ ns, and a curved front at $t = 4.7$ ns. According to the simulation the shock front appears nearly flat in the time interval $t = 1.7$–3.5 ns.

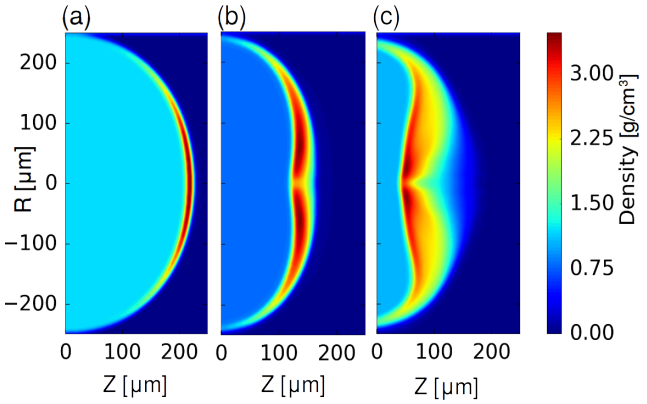

FIG. 16. DUED simulation of the hemispherical target. Simulated density maps at three selected times: (a) $t = 0.7$ ns; (b) $t = 2.7$ ns; (c) $t = 4.7$ ns.

IV. CONCLUSION

We presented experimental results on the generation of strong shock waves, using targets with flat and hemispherical interaction surfaces. The aim was to show that, performing a proper treatment of the experimental raw data, X-ray radiography can provide valuable information concerning the shape of the shock front and, under certain conditions, the density map of the shocked target region. Experimental radiographs were favourably compared with synthetic radiographs using data generated by DUED simulations. A quantitative comparison however requires that a detailed knowledge of the actual laser intensity distribution in the focal spot is included in the code.

ACKNOWLEDGMENTS

This work benefitted from the support of COST Action MP1208 'Developing the physics and the Scientific Community for Inertial Fusion', the Italian MIUR grant No. PRIN 2012AY5LEL and Sapienza University (Grant 2015 C26A15YTMA), and by the Eurofusion consortium. The experiment leading to these results received funding from Laserlab-Europe (grant agreement No. 284464, EU's Seventh Framework Programme). We thank T. Vinci for discussions on EOS data and V. Tikhonchuk for a critical appraisal of the manuscripts. We thank an anonymous referee for pointing out a mistake in a previous version of Fig. 4.

[1] R. J. Trainor, J. W. Shaner, J. M. Auerbach, and N. C. Holmes, Physical Review Letters **42**, 1154 (1979).

[2] A. Benuzzi, T. Löwer, M. Koenig, B. Faral, D. Batani, D. Beretta, C. Danson, and D. Pepler, Physical Review

E **54**, 2162 (1996).
[3] D. Batani, L. Antonelli, S. Atzeni, J. Badziak, F. Baffigi, T. Chodukowski, F. Consoli, G. Cristoforetti, R. De Angelis, R. Dudzak, *et al.*, Physics of Plasmas (1994-present) **21**, 032710 (2014).
[4] R. Nora, W. Theobald, R. Betti, F. Marshall, D. Michel, W. Seka, B. Yaakobi, M. Lafon, C. Stoeckl, J. Delettrez, *et al.*, Physical review letters **114**, 045001 (2015).
[5] D. Batani, EPL (Europhysics Letters) **114**, 65001 (2016).
[6] M. Koenig, A. Benuzzi-Mounaix, A. Ravasio, T. Vinci, N. Ozaki, S. Lepape, D. Batani, G. Huser, T. Hall, D. Hicks, *et al.*, Plasma physics and controlled fusion **47**, B441 (2005).
[7] G. Collins, L. Da Silva, P. Celliers, D. Gold, M. Foord, R. Wallace, A. Ng, S. Weber, K. Budil, and R. Cauble, Science **281**, 1178 (1998).
[8] M. K. Matzen, M. Sweeney, R. Adams, J. Asay, J. Bailey, G. Bennett, D. Bliss, D. Bloomquist, T. Brunner, R. Campbell, *et al.*, Physics of Plasmas (1994-present) **12**, 055503 (2005).
[9] A. Benuzzi-Mounaix, M. Koenig, A. Ravasio, T. Vinci, N. Ozaki, M. R. le Gloahec, B. Loupias, G. Huser, E. Henry, S. Bouquet, *et al.*, Plasma physics and controlled fusion **48**, B347 (2006).
[10] A. Ravasio, M. Koenig, S. Le Pape, A. Benuzzi-Mounaix, H. Park, C. Cecchetti, P. Patel, A. Schiavi, N. Ozaki, A. Mackinnon, *et al.*, Physics of Plasmas (1994-present) **15**, 060701 (2008).
[11] A. Benuzzi-Mounaix, B. Loupias, M. Koenig, A. Ravasio, N. Ozaki, M. R. Le Gloahec, T. Vinci, Y. Aglitskiy, A. Faenov, T. Pikuz, *et al.*, Physical Review E **77**, 045402 (2008).
[12] E. Brambrink, H. Wei, B. Barbrel, P. Audebert, A. Benuzzi-Mounaix, T. Boehly, T. Endo, C. Gregory, T. Kimura, R. Kodama, *et al.*, Physical Review E **80**, 056407 (2009).
[13] A. Morace, L. Fedeli, D. Batani, S. Baton, F. Beg, S. Hulin, L. Jarrot, A. Margarit, M. Nakai, P. Nakatsutsumi, P. Nicolai, N. Piovella, M. Wei, X. Vaisseau, L. Volpe, and J. Santos, Physics of Plasmas (1994-present) **21**, 102712 (2014).
[14] S. X. Hu, V. A. Smalyuk, V. N. Goncharov, J. P. Knauer, P. B. Radha, I. V. Igumenshchev, J. A. Marozas, C. Stoeckl, B. Yaakobi, D. Shvarts, T. C. Sangster, P. W. McKenty, D. D. Meyerhofer, S. Skupsky, and R. L. McCrory, Physical Review Letters **100**, 185003 (2008).
[15] S. Le Pape, A. Macphee, D. Hey, P. Patel, A. Mackinnon, M. Key, J. Pasley, M. Wei, S. Chen, T. Ma, F. Beg, N. Alexander, R. Stephens, D. Offerman, A. Link, L. Van-Woerkom, and R. Freeman, Review of Scientific Instruments **79**, 106104 (2008).
[16] D. G. Hicks, B. K. Spears, D. G. Braun, R. E. Olson, C. M. Sorce, P. M. Celliers, G. W. Collins, and O. L. Landen, Review of Scientific Instruments **81**, 10E304 (2010).
[17] A. L. Kritcher, T. Doëpnner, D. Swift, J. Hawreliak, G. Collins, J. Nilsen, B. Bachmann, E. Dewald, D. Strozzi, S. Felker, O. N. Landen, O. Jones, C. Thomas, J. Hammer, C. Keane, H. J. Lee, S. H. Glenzer, S. Rothman, D. Chapman, D. Kraus, P. Neumayer, and R. W. Falcone, High Energy Density Physics **10**, 27 (2014).
[18] S. Atzeni, A. Schiavi, F. Califano, F. Cattani, F. Cornolti, D. Del Sarto, T. Liseykina, A. Macchi, and F. Pegoraro, Computer Physics Communications **169**, 153 (2005).
[19] L. M. Barker and R. E. Hollenbach, Journal of Applied Physics **43**, 4669 (1972).
[20] L. von Hamos, Naturwissenschaften **20** (1932).
[21] L. von Hamos, Annalen der Physik (Leipzig) **17** (1933).
[22] F. Marshall, P. McKenty, J. Delettrez, R. Epstein, J. Knauer, V. Smalyuk, J. Frenje, C. Li, R. Petrasso, F. Séguin, *et al.*, Physical review letters **102**, 185004 (2009).
[23] J. H. Hubbell and S. M. Seltzer, *Tables of X-ray mass attenuation coefficients and mass energy-absorption coefficients 1 keV to 20 MeV for elements Z= 1 to 92 and 48 additional substances of dosimetric interest*, Tech. Rep. (National Inst. of Standards and Technology-PL, Gaithersburg, MD (United States). Ionizing Radiation Div., 1995).
[24] S. Atzeni, A. Caruso, and V. Pais, Laser and Particle Beams **4**, 393 (1986).
[25] M. Barrios, D. Hicks, T. Boehly, D. Fratanduono, J. Eggert, P. Celliers, G. Collins, and D. Meyerhofer, Physics of Plasmas (1994-present) **17**, 056307 (2010).
[26] K. Eidmann, Laser and Particle Beams **12**, 223 (1994).
[27] R. B. Stephens, R. A. Snavely, Y. Aglitskiy, F. Amiranoff, C. Andersen, D. Batani, S. D. Baton, T. Cowan, R. R. Freeman, T. Hall, S. P. Hatchett, J. M. Hill, M. H. Key, J. A. King, J. A. Koch, M. Koenig, A. J. MacKinnon, K. L. Lancaster, E. Martinolli, P. Norreys, E. Perelli-Cippo, M. Rabec Le Gloahec, C. Rousseaux, J. J. Santos, and F. Scianitti, Physical Review E **69**, 066414 (2004).